

Robust determination of the fibre orientation distribution in diffusion MRI: Non-negativity constrained super-resolved spherical deconvolution

J-Donald Tournier,^{*} Fernando Calamante, and Alan Connelly

Brain Research Institute, Melbourne, Australia

Department of Medicine, University of Melbourne, Melbourne, Australia

Received 12 September 2006; revised 13 December 2006; accepted 10 February 2007

Available online 21 February 2007

Diffusion-weighted (DW) MR images contain information about the orientation of brain white matter fibres that potentially can be used to study human brain connectivity *in vivo* using tractography techniques. Currently, the diffusion tensor model is widely used to extract fibre directions from DW-MRI data, but fails in regions containing multiple fibre orientations. The spherical deconvolution technique has recently been proposed to address this limitation. It provides an estimate of the fibre orientation distribution (FOD) by assuming the DW signal measured from any fibre bundle is adequately described by a single response function. However, the deconvolution is ill-conditioned and susceptible to noise contamination. This tends to introduce artefactual negative regions in the FOD, which are clearly physically impossible. In this study, the introduction of a constraint on such negative regions is proposed to improve the conditioning of the spherical deconvolution. This approach is shown to provide FOD estimates that are robust to noise whilst preserving angular resolution. The approach also permits the use of super-resolution, whereby more FOD parameters are estimated than were actually measured, improving the angular resolution of the results. The method provides much better defined fibre orientation estimates, and allows orientations to be resolved that are separated by smaller angles than previously possible. This should allow tractography algorithms to be designed that are able to track reliably through crossing fibre regions.

© 2007 Elsevier Inc. All rights reserved.

Introduction

The diffusion tensor model is currently the mathematical framework most widely used to relate the diffusion-weighted magnetic resonance imaging (DW-MRI) signal to the underlying diffusion process, and provides a number of useful parameters

(Basser et al., 1994). Of particular significance is the major eigenvector of the diffusion tensor, corresponding to the direction of fastest diffusion (Basser, 1995). The direction of this vector has been shown to correspond well with the orientation of the fibres in a number of major white matter structures, such as the optic tract of the rat (Lin et al., 2003). Based on this premise, a number of tractography algorithms have been proposed to map the path of white matter tracts in the brain (e.g. Mori et al., 1999; Conturo; et al., 1999; Parker et al., 2002; Behrens et al., 2003; Tournier et al., 2003). Most of these techniques rely on the diffusion tensor model to provide an accurate estimate of the white matter fibre orientation.

Unfortunately, the diffusion tensor model is not always adequate, particularly in voxels containing contributions from differently oriented fibre bundles (Alexander et al., 2002; Frank, 2002; Tuch et al., 2002; Behrens et al., 2007). The reason for this is two-fold. First, the diffusion tensor model is only strictly valid for free diffusion, and is therefore only an approximation for the *in vivo* case. Second, and more importantly, the diffusion tensor can only possess a single maximum, and is therefore unable to adequately characterise a system consisting of several distinct fibre orientations. At the resolution currently achievable with DW-MRI, a large number of voxels will contain contributions from different bundles with distinct orientations, where the diffusion tensor model will provide a poor fit to the data (Alexander et al., 2002). In particular, the major eigenvector will in general no longer correspond to the orientation of any of the fibre tracts present (Assaf et al., 2004). It should be emphasised that a significant proportion of white matter voxels are affected by this problem. A recent study estimates that one third of white matter voxels contain more than one fibre population (Behrens et al., 2007). Moreover, many of the major tracts in the brain do pass through regions containing multiple fibre populations at some point along their path, causing tractography applications that rely on the diffusion tensor model to provide unreliable results if the tracks produced happen to venture into affected voxels (Pierpaoli et al., 2001).

^{*} Corresponding author. Brain Research Institute, Neurosciences Building, Austin Health, Banksia Street, Heidelberg West, Victoria 3081, Australia. Fax: +61 3 9496 4071.

E-mail address: d.tournier@brain.org.au (J.-D. Tournier).

Available online on ScienceDirect (www.sciencedirect.com).

We recently presented a technique that is capable of estimating the distribution of fibre orientations within each voxel directly from the diffusion-weighted (DW) data, using the concept of spherical deconvolution (Tournier et al., 2004). A number of other approaches have also been proposed to address this issue, but there are some inherent limitations with each of them. Q-ball imaging (Tuch, 2004), diffusion spectrum imaging (DSI) (Wedeen et al., 2005) and the CHARMED model (Assaf et al., 2004) all require large b -values that are difficult to obtain on a clinical system. Moreover, DSI and CHARMED both require a wide range of b -values, leading to impractical scan times. PAS-MRI (Jansons and Alexander, 2003) is very computer-intensive, which limits its widespread practical use. The recently proposed diffusion orientation transform (Özarslan et al., 2006) assumes monoexponential signal decay, which has been shown to be not valid for high q -values *in vivo* (Cohen and Assaf, 2002). It is worth noting that these techniques are all rooted in the q -space formalism (Callaghan et al., 1988) and thus provide an approximation to the spin propagator (or more commonly just its angular dependence), rather than the fibre orientations themselves. Although the two are clearly related, there may be cases where that relationship is not straightforward (for example, fibres crossing at angles other than 90° (Zhan and Yang, 2006)).

Multiple tensor fitting algorithms (Tuch et al., 2002; Hosey et al., 2005; Behrens et al., 2007) provide discrete fibre orientations, but tend to perform poorly when more than two fibre orientations are present. FORECAST (Anderson, 2005) is a generalisation of multiple tensor fitting, and is in essence a spherical deconvolution; we anticipate that it would also benefit from the modifications proposed here.

The spherical deconvolution technique that we proposed is not affected by the problems mentioned above. However, like most deconvolution problems, this method is ill-posed and susceptible to noise. In this study, we present a novel iterative method to perform the spherical deconvolution that preserves the angular resolution while remaining robust to noise effects. This is done by placing a non-negativity constraint of the estimated FOD, as negative fibre orientation densities are physically impossible. This constraint eliminates the need for low-pass filtering, and indeed provides enough prior information to estimate the FOD with a higher resolution than would otherwise be possible from the data alone (this is known as super-resolution; Starck et al., 2002). The method is described below, and its accuracy and precision are assessed using simulations and *in vivo* data (including a bootstrap analysis; Jones, 2003).

Theory

Spherical deconvolution

The method of spherical deconvolution (Tournier et al., 2004) can be used to estimate the distribution of fibre orientations present within each imaging voxel. With this method, the signal measured during a high angular resolution DW imaging experiment can be expressed as the convolution over spherical coordinates of the response function with the fibre orientation distribution (FOD). The response function describes the DW signal intensity that would be measured as a function of orientation for a single fibre bundle aligned along the z -axis. The FOD contains all the desired information regarding both the orientations of the various fibre populations that may be present, including the uncertainty around

each of these estimated orientations, and their respective volume fractions. The FOD can be estimated by performing the reverse spherical deconvolution operation, which can be performed efficiently using spherical and rotational harmonics, using the spherical space equivalent of the Cartesian space Fourier convolution theorem (Healy et al., 1998).

In the spherical harmonics (SH) framework, the convolution operation is performed as follows. For each harmonic order l , the SH coefficients of the signal profile $S(\theta, \phi)$ and the FOD $F(\theta, \phi)$ are written as vectors s_l and f_l of length $2l+1$, whereas the rotational harmonic coefficients of the convolution kernel $R(\theta, \phi, \varphi)$ (the response function) are written as a matrix \mathbf{R}_l of size $(2l+1) \times (2l+1)$. The convolution operation then simply consists of one matrix multiplication per harmonic order l :

$$s_l = \mathbf{R}_l \cdot f_l \quad (1)$$

The spherical deconvolution operation can be performed by simple matrix inversion. More details can be found in Appendix A.

However, the spherical deconvolution problem is ill-posed and thus susceptible to noise. This effect can be minimised to some extent at the expense of angular resolution by using low-pass filtering, whereby the high angular frequency components in the FOD are attenuated or eliminated (Tournier et al., 2004).

This unconstrained, low-pass filtered implementation of the method will be referred to simply as *filtered spherical deconvolution* (filtered SD) for the remainder of this work.

Non-negativity constraint

Without low-pass filtering, the noise will introduce large spurious negative lobes in the reconstructed FOD, which are clearly physically impossible. This provides an alternative way of reducing the ill-conditioning of the technique, by adding a constraint on the presence of these negative values in the FOD, rather than filtering out the high angular frequencies. Most white matter voxels are expected to contain contributions from relatively few fibre bundles. Therefore, apart from a few well-defined peaks (corresponding to the fibre orientations), we expect the FOD to be zero over most of its support. As a result, eliminating any negative values in these regions must also strongly reduce the high frequency noise that generated them.

This method will be referred to as *constrained spherical deconvolution* (CSD) for the remainder of this work.

Optimisation procedure

In this study, the constraint on negative values was applied using a modified Tikhonov regularisation method (Hansen, 1994). It should be made clear that this approach penalises negative FOD values, but does not completely forbid them: the constraint is not applied strictly. In brief, the method involves the following steps. First, an initial estimate of the FOD is obtained. A set of directions is then identified, along which the FOD amplitude is negative. This information is then incorporated as a Tikhonov constraint, driving the amplitude of the FOD along those orientations to zero. An improved estimate of the FOD is then obtained by solving the Tikhonov problem, providing a new set of negative amplitude directions. The procedure is repeated until convergence is achieved. Each step is explained in more detail below.

In its original formulation, Tikhonov regularisation involves the minimisation of the weighted sum of two terms (Hansen, 1994):

$$\|\mathbf{A}\mathbf{f} - \mathbf{b}\|^2 + \lambda^2 \|\mathbf{L}(\mathbf{f} - \mathbf{f}')\|^2 \quad (2)$$

The first term corresponds to the data-driven part, and is a simple linear least-square fit of the solution \mathbf{f} (the parameters to be estimated) to the data \mathbf{b} , via the problem matrix \mathbf{A} . The second term is the regularisation part, given by the norm of \mathbf{f} relative to an initial estimate \mathbf{f}' , multiplied by the constraint matrix \mathbf{L} . The regularisation parameter λ controls the relative weighting between these two terms. With $\lambda=0$, the problem reduces to the initial linear least-squares fit. As $\lambda \rightarrow \infty$, the regularisation term begins to dominate, and the solution tends to \mathbf{f}' .

In the context of spherical deconvolution, \mathbf{f} corresponds to the SH coefficients of the FOD, \mathbf{b} corresponds to the measured signal intensities, and the problem matrix \mathbf{A} is:

$$\mathbf{A} = \mathbf{Q}\mathbf{R} \quad (3)$$

where \mathbf{Q} maps spherical harmonic coefficients to the corresponding intensities along the DW directions, and \mathbf{R} performs the spherical convolution with the kernel $R(\theta)$ (details can be found in the Appendix A).

In this study, \mathbf{f}' was set to zero, and the constraint matrix \mathbf{L} that was used maps \mathbf{f} (i.e. the SH coefficients of the FOD) onto a set of orientations along which the FOD is assumed to have zero amplitude. Since these directions are unknown *a priori*, the approach used in this study was to iteratively refine an initial estimate of this set of directions, as follows.

First, \mathbf{f}_0 , an initial estimate of the FOD is obtained using filtered SD. Since this initial estimate is not critical, here the SH series was simply truncated at harmonic order $l_{\max}=4$. Note that results shown in this study that were produced directly using the filtered SD method itself were derived using filtering parameters optimised independently for each data set (see Methods below).

Next, the amplitude \mathbf{u} of the FOD is computed along a large set of N uniformly distributed directions (in our case, $N=300$, calculated using an electrostatic repulsion model (Jones et al., 1999)):

$$\mathbf{u} = \mathbf{P}\mathbf{f}_i \quad (4)$$

where \mathbf{P} maps \mathbf{f}_i (i.e. the SH coefficients of the current FOD estimate) onto the amplitudes \mathbf{u} along the N directions (see Appendix A). \mathbf{L} is then formed as follows:

$$\mathbf{L}_{m,n} = \begin{cases} \mathbf{P}_{m,n} & \mathbf{u}_m < \tau \\ 0 & \mathbf{u}_m \geq \tau \end{cases} \quad (5)$$

where τ is a user-specified threshold, controlling the amplitude below which the corresponding fibre orientation density is assumed to be zero. Ideally, τ should be set to zero. However, to improve the stability of the algorithm, τ was set to 10% of the mean FOD amplitude (see Super-resolution).

\mathbf{L} therefore provides the amplitude of the current estimate of the FOD for the set of directions along which that amplitude is below the threshold, τ . An improved estimate of the FOD is then obtained by assuming that the fibre density along these directions should be zero, and thus by solving:

$$\mathbf{f}_{i+1} = \arg \min \{ \|\mathbf{A}\mathbf{f}_i - \mathbf{b}\|^2 + \lambda^2 \|\mathbf{L}\mathbf{f}_i\|^2 \} \quad (6)$$

This improved FOD \mathbf{f}_{i+1} is then used to form a new matrix \mathbf{L} using Eqs. (4) and (5), and the process is repeated until there is no

further change in the matrix \mathbf{L} ; in other words, until the set of directions that can be assumed to have zero fibre density is established. This was typically reached within 5 to 10 iterations, with little or no dependence on parameters such as λ , τ , l_{\max} or SNR.

Super-resolution

Using prior information allows the possibility of estimating more parameters than actual measurements (a concept known as super-resolution; Starck et al., 2002), provided that the amount of prior information is sufficient to constrain the additional degrees of freedom. The reason for this can be appreciated by expressing Eq. (6) as follows:

$$\begin{aligned} \mathbf{x}_{i+1} &= \arg \min \left\{ \left\| \begin{pmatrix} \mathbf{A} \\ \lambda \mathbf{L} \end{pmatrix} \mathbf{f}_i - \begin{pmatrix} \mathbf{b} \\ 0 \end{pmatrix} \right\|^2 \right\} \\ &= \arg \min \{ \|\mathbf{M}\mathbf{f}_i - \mathbf{b}'\|^2 \} \end{aligned} \quad (7)$$

where $\mathbf{M} = \begin{pmatrix} \mathbf{A} \\ \lambda \mathbf{L} \end{pmatrix}$ and $\mathbf{b}' = \begin{pmatrix} \mathbf{b} \\ 0 \end{pmatrix}$

It is clear from Eq. (7) that the problem can be solved as long as the matrix \mathbf{M} is always square or over-determined. This requirement is fulfilled as long as the number of rows of \mathbf{L} (the number of assumed zero-amplitude directions) is always greater than the difference between the number of columns and the number of rows of \mathbf{A} . For example, using 60 DW directions, it is possible to estimate the 91 SH coefficients required for harmonic order $l_{\max}=12$ provided that the number of directions along which the fibre density can be assumed to be zero never falls below 31 (i.e. 91–60) at each iteration.

This variant of CSD will be referred to as *super-resolved constrained spherical deconvolution* (super-CSD) for the remainder of this work.

Methods

Response function estimation

As mentioned in the Theory section, spherical deconvolution requires an estimate of the response function, corresponding to the DW signal that would be measured as a function of orientation for a single white matter fibre bundle aligned with the z -axis. Although the diffusion tensor model provides a good fit to the DW signal for a single fibre population at low b -values, it has been shown to deviate significantly at higher b -values (Mulkern et al., 1999; Clark and Le Bihan, 2001). Therefore, the response functions used in this study were measured from the DW data themselves, as described below. As a consequence, simulations were performed only for those b -values that were used to acquire *in vivo* data and for which a response function could be measured ($b=1000$ and 3000 s/mm² in this study).

Each of the response functions used was measured from one of the DW data sets using the following procedure (as in Tournier et al., 2004). First, the 300 white matter voxels with the highest fractional anisotropy (Basser, 1995) were identified, as they could each be assumed to contain a single fibre population. For each voxel, the DW signal intensity profiles were fit to the tensor model, from which the major eigenvector was computed. The orientation of the major eigenvector was then used to calculate the rotation angle required to re-orient the estimated fibre orientation with the

z-axis. A modified DW encoding scheme was then generated by applying this rotation to each orientation in the DW scheme. Finally, the SH coefficients of the rotated DW signal were computed by performing the SH transform assuming this modified DW encoding scheme. Performing this procedure independently in each relevant voxel provides a good estimate of the SH coefficients of the individual DW signal profiles, each re-aligned with the z-axis. Finally, the SH coefficients were averaged over all voxels in the ROI, and all $m \neq 0$ coefficients were set to zero (due to the assumed axial symmetry of the response function; Tournier et al., 2004). This provides a good estimate of the response function in spherical harmonics, from which the corresponding rotational harmonic coefficients can easily be computed (see Appendix A).

All *in vivo* results, including the bootstrap results, were generated using the response function estimated from the corresponding DW data set. For the simulations, the response function used to generate the $b=3000$ s/mm² results was obtained using data set A (see below), while that for the $b=1000$ s/mm² results was obtained using data set C (see below). The filtering parameters used for filtered SD were optimised independently for each data set using a minimum entropy method that we presented recently (Tournier et al., 2005).

Simulations

The accuracy and precision of the CSD method were assessed using numerical simulations for a range of different conditions and parameters, including b -value, SNR, separation angle, λ , τ and l_{\max} . First, a system of two fibre populations crossing at various separation angles was simulated, assuming the appropriate response function (see above), from which the noise-free DW signal was computed along 60 uniformly distributed directions. Rician noise was then added to each DW signal, and these data were processed using either filtered SD or CSD to produce an estimate of the FOD. This last step was repeated 100 times to compute mean and standard deviations for each estimated fibre orientation. In addition, the orientations of both peaks were extracted from each computed FOD, using an implementation of Newton's method adapted for spherical coordinates. In order to avoid local maxima, the peak search was re-started from 100 uniformly distributed orientations, and the two largest peaks found over the 100 re-starts were selected.

Performance was quantified using two measures based on the estimated peak orientations. The average orientation error was computed as the 95% confidence interval of the angle between the estimated and true fibre orientations. The success rate was computed as the proportion of computed FODs where two distinct peaks were clearly identified by the peak finding algorithm; the condition for this was that the amplitude of the second peak was at least 20% that of the largest peak.

Bootstrap analysis

Recent studies have shown the potential of the bootstrap method to estimate the reproducibility of *in vivo* white matter orientations derived from diffusion-tensor MRI (Jones, 2003). This can be applied to any DW MRI analysis technique. The method requires the acquisition of N repeats (in our case, $N=3$) of a complete DW data set, so that N samples are available for each DW direction. A sample DW data set can then be produced by randomly selecting one of the N available samples for each direc-

tion. In this way, a full DW data set is produced from a random combination of the images in the N repeats of the original data set, which can then be processed using the method under investigation. In this study, CSD (and the super-CSD variant) was compared to filtered SD.

In order to produce meaningful and easily interpreted measures of reproducibility, the orientations provided by spherical deconvolution were estimated from the FOD using a peak-finding algorithm (as described above). However, there are disadvantages with this procedure. First, much of the information contained in the FOD is discarded. One of the strengths of spherical deconvolution is that it provides an estimate of the distribution of fibre orientations, rather than just a set of discrete orientations. There is valuable information in the distribution itself that can be used for fibre tracking, for example using probabilistic streamlines techniques (Behrens et al., 2003, 2007; Parker and Alexander, 2005), or to help differentiate crossing and 'kissing' fibre arrangements (Hong et al., 2006). Second, extracting peak orientations is only valid if the FOD contains a small number of discrete orientations, with no significant curvature or 'fanning' at the voxel level. For this latter reason, the bootstrap analysis was restricted to a region of the brain containing two discrete white matter orientations (shown in Results, Fig. 7).

The bootstrap method was used to produce 500 sample DW data sets. For each data set, the FODs were estimated, from which the peak orientations were extracted. Finally, the 95% confidence intervals for the orientation of each peak were computed within each voxel, and displayed as 'cones of uncertainty' (Jones, 2003).

Data acquisition

To investigate the effectiveness of the proposed method, it was performed on four different data sets acquired on 3 different MRI scanners. The first two (sets A and B) were acquired using a relatively high b -value (~ 3000 s/mm²), the last two (sets C and D) using a more typical clinical b -value of around 1000 s/mm². Data set B consisted of 3 identical repeats to allow bootstrap analyses to be performed (see above). Data set D employed a 20 DW direction scheme designed for diffusion tensor studies, and was included to assess the performance of the proposed method with data that would not normally be deemed suitable for spherical deconvolution. All SNR values quoted were calculated as S/σ , where S is the $b=0$ signal within a region of interest in the vicinity of the basal ganglia, and σ was estimated as $\sqrt{1/2} \times$ standard deviation of the difference between two $b=0$ images over the same region of interest.

Data set A was acquired from a healthy volunteer on a 1.5T Siemens Avanto system, using an eddy-current-nulled twice-refocused EPI sequence (Reese et al., 2003) (b -value=3000 s/mm², TE=128 ms, 60 DW directions, in-plane resolution 2.1×2.1 mm², 3 mm slice thickness, 37 contiguous axial slices, SNR($b=0$) ~ 18 , acquisition time ~ 9 min).

Data set B was acquired from a healthy volunteer on a 1.5T Siemens Vision system, also using an eddy-current-nulled twice-refocused EPI sequence (Reese et al., 2003) (b -value=2971 s/mm², TE=140 ms, 60 DW directions, in-plane resolution 3×3 mm² zero-filled to 1.5×1.5 mm², 3 mm slice thickness, 40 contiguous axial slices, SNR($b=0$) ~ 21 , 3 repeats, total acquisition time ~ 75 min). Due to the long scan time, motion correction was required. However, standard realignment methods could not be used due to the low SNR of the DW images. The following approach was therefore

used. A non-DW volume was acquired at the start of the scan, and after every 10 DW volumes. The non-DW volumes were co-registered using rigid body transformations, and each DW volume was then realigned by applying a transform obtained by linear interpolation from the transforms of the two nearest non-DW volumes. Realignment parameters were estimated using the FLIRT program from the FMRIB Software Library (Oxford Centre for Functional Magnetic Resonance Imaging of the Brain, Oxford, UK).

Data set C was acquired from a healthy volunteer on a 1.5T GE Signa Echospeed scanner, using a cardiac-gated single spin-echo EPI sequence (b -value=1000 s/mm², TE=95 ms, 60 DW directions, in-plane resolution 2.5×2.5 mm² zero-filled to 1.875×1.875 mm², 2.5 mm slice thickness, 42 contiguous axial slices, SNR($b=0$)~19). Eddy-current correction was performed using a 2D image registration technique (Symms et al., 1997).

Data set D was acquired from a healthy volunteer on a 1.5T Siemens Avanto system, using an eddy-current-nulled twice-refocused EPI sequence (Reese et al., 2003) (b -value=1000 s/mm², TE=89 ms, 20 DW directions, in-plane resolution 2.5×2.5 mm², 2.5 mm slice thickness, 45 contiguous axial slices, 2 averages, SNR($b=0$)~31 (after averaging), acquisition time ~4 1/2 min).

Results

Optimisation of regularisation parameters

The threshold parameter τ determines which orientations are assumed to have zero fibre density. Ideally, this would be set to zero. However, with super-CSD, the algorithm may fail to converge if the number of zero-amplitude directions identified falls below the minimum required. This was found to occur frequently with $\tau=0$, particularly in grey matter regions. Setting τ to a value greater than zero improves the stability of the algorithm, by allowing more directions to be identified as having zero fibre density. It was found that setting τ to 10% of the mean initial FOD amplitude drastically improved the convergence of

the algorithm, with minimal impact on the quality of the results (Fig. 1).

The relative weighting of the constraint is controlled by the regularisation parameter λ . For low values of λ , the estimated FOD is relatively sensitive to noise and still contains significant negative lobes (Fig. 1). For larger λ , the FOD is more robustly estimated with the negative lobes decreasing almost to zero, but this comes at the expense of a slight reduction in angular resolution, resulting in slightly broader peaks. Therefore, in this study, the regularisation parameter λ was set empirically to the smallest value that would achieve negative lobe amplitudes that were negligible compared to that of the dominant peaks ($\lambda=1$; see Fig. 1).

Based on these results, the parameters were set to $\lambda=1$ and $\tau=10\%$ of the mean initial FOD amplitude for the remainder of this study.

Simulations

The simulations show that for parameters typical of *in vivo* data sets, CSD can resolve fibre orientations separated by smaller angles than can be resolved with filtered SD, and with no increase in the noise sensitivity. For the experimental conditions simulated, CSD can resolve fibre populations separated by angles as small as 40°, compared with 60° for filtered SD (Fig. 2). Angular resolution increases with increasing l_{\max} : the FODs estimated with super-CSD have sharper features, and fibre orientations separated by smaller angles can be resolved (Fig. 2). Importantly, introducing the non-negativity constraint in the spherical deconvolution does not introduce any bias in the estimated orientations (Fig. 3).

The variance in the FOD is lowest when the two fibre populations are well separated, and shows a slight tendency to increase as l_{\max} is increased (Fig. 2). As expected, increasing the SNR reduces the variance in the FOD (Fig. 3). The variance is also lower at $b=3000$ s/mm² (Fig. 2, row 4) than at $b=1000$ s/mm² (Fig. 4).

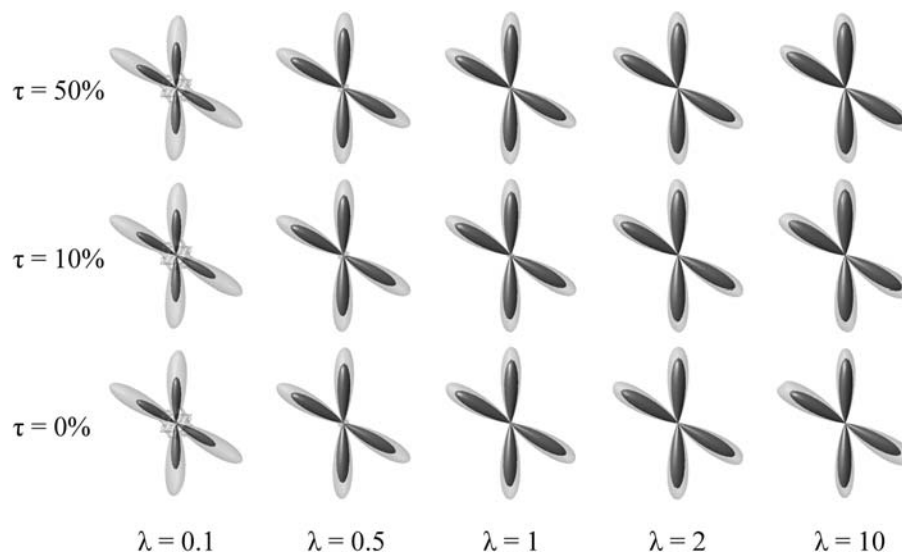


Fig. 1. Effect of the regularisation parameter λ and the threshold τ on the reconstructed FOD obtained using super-CSD with $l_{\max}=12$. The opaque surface corresponds to the mean FOD over 100 noise realisations, whereas the transparent surface corresponds to the mean + 2 standard deviations. Other parameters were SNR=30, b -value=3000 s/mm², 60 DW directions, separation angle=60°.

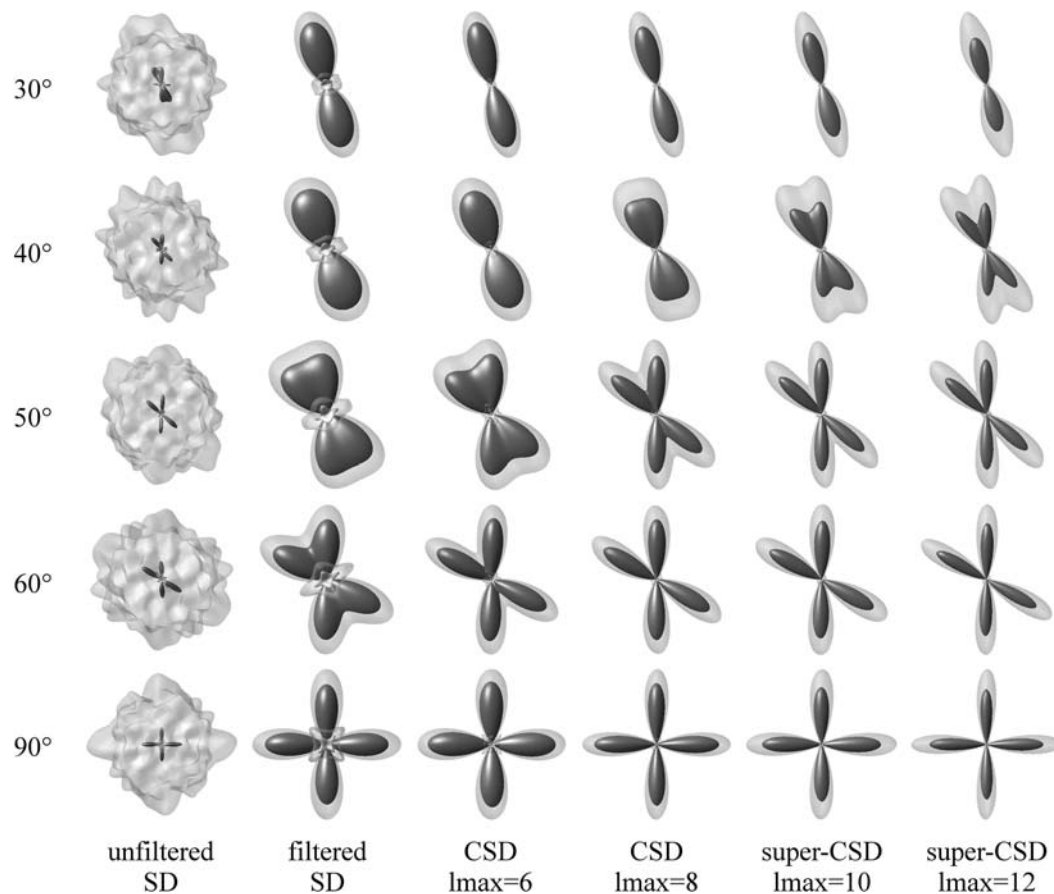


Fig. 2. Effect of separation angle and l_{\max} on the reconstructed FOD. The opaque surface corresponds to the mean FOD over 100 noise realisations, whereas the transparent surface corresponds to the mean + 2 standard deviations. Other parameters were SNR=20, b -value=3000 s/mm², 60 DW directions, $\lambda=1$, $\tau=10\%$ of mean initial FOD amplitude.

The 95% confidence interval (CI) for the peak orientations is reduced at higher SNR: it is almost halved by increasing the SNR from 20 to 30 at both b -values investigated (Fig. 5). The 95% CI is also lower at the higher b -value investigated: with SNR=30 and $l_{\max}=10$, it is almost halved from 9° at $b=1000$ s/mm² to approximately 5° at $b=3000$ s/mm². Using a larger number of directions also reduces the 95% CI: at SNR 30, $b=1000$ s/mm², the 95% CI is halved by increasing the number of DW directions from 20 to 60 (Fig. 6).

The precision of the estimated fibre orientations extracted by peak finding is highest when the two fibre orientations are well separated: the 95% CI generally increases as the separation angle decreases away from 90° (Fig. 6). With 60 DW directions and a 50° separation angle, the smallest 95% CI is achieved using super-CSD with $l_{\max}=10$ at both b -values (with the exception of the SNR=20 case) (Fig. 5). With a 90° separation angle, a smaller 95% CI is observed (3.5° at $b=3000$ s/mm² and SNR=30, as opposed to 5° for a 50° separation angle), but in this case the smallest 95% CI is achieved using CSD with $l_{\max}=8$ (Fig. 6).

The minimum angle that can be successfully resolved is reduced by using CSD, and decreases further as l_{\max} is increased (Fig. 6). With 60 DW directions and SNR=30, the smallest angle that can be resolved with 95% success is 40° with $l_{\max}=16$ at both b -values (Fig. 6). With 20 DW directions and SNR=30, the smallest angle that can be resolved with 95% success is 45° with $l_{\max}=16$ and $b=1000$ s/mm² (Fig. 6).

In vivo data: bootstrap analysis

The bootstrap analysis of data set B confirms many of the findings of the simulations. CSD can provide more precise estimates of the fibre orientations than filtered SD (Fig. 7 and Table 1), particularly when the fibres are separated by a small angle. Again, all methods provide more robust peak orientation estimates for wider separation angles. For CSD, the optimal value of l_{\max} depends on the separation angle between the two fibre orientations: for shallow angles, super-CSD with $l_{\max}=10$ is most robust, whereas for wider angles, CSD with $l_{\max}=8$ is most robust.

In vivo data: visual inspection

The *in vivo* results are consistent both with the simulations and with the bootstrap analysis. The fibre orientations estimated in the region of the centrum semiovale are consistent with known anatomy; the corona radiata, superior longitudinal fasciculus and commissural fibres can all be clearly identified. As expected, the FODs obtained using CSD and particularly with super-CSD show an increase in angular resolution with more clearly defined peaks (Figs. 8, 9 and 10). Also, the results obtained with $b=1000$ s/mm² (see highlighted region in Fig. 9) are qualitatively more sensitive to noise (i.e. there are more noise-induced spurious peaks) than those obtained at $b=3000$ s/mm² (Fig. 8).

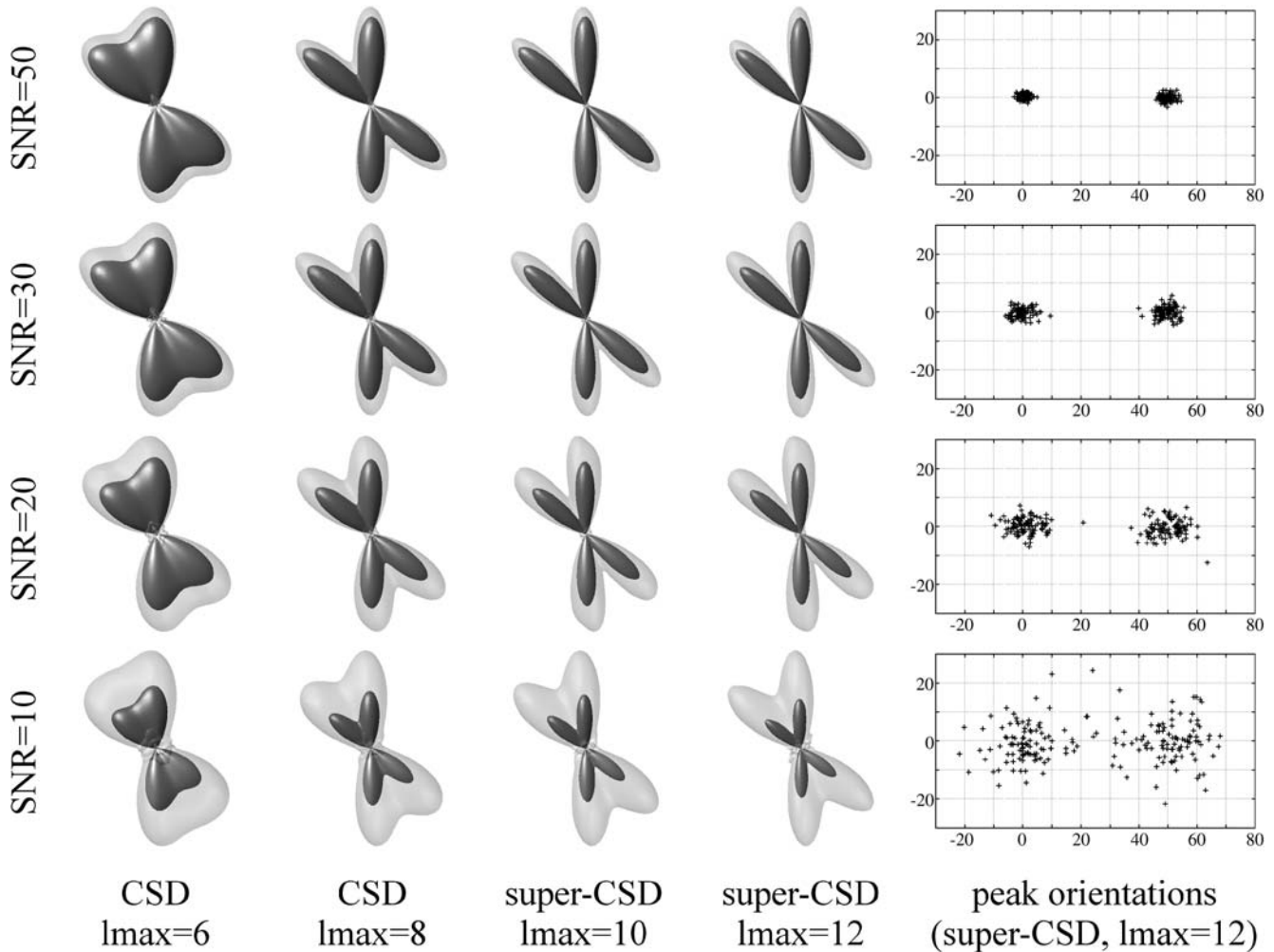


Fig. 3. Effect of SNR and l_{\max} on the reconstructed FOD. The opaque surface corresponds to the mean FOD over 100 noise realisations, whereas the transparent surface corresponds to the mean +2 standard deviations. Right: plots of peak orientations for super-CSD with $l_{\max}=12$ (x-axis: azimuth, y-axis: elevation, both in degrees). Other parameters were separation angle = 50° , b -value = 3000 s/mm^2 , 60 DW directions, $\lambda=1$, $\tau=10\%$ of mean initial FOD amplitude.

The results shown in Fig. 10 were produced from data set D, which was acquired using a 20 DW direction scheme tailored for diffusion tensor analysis. Remarkably, the FODs obtained using CSD and in particular super-CSD show good angular resolution and noise sensitivity, and are consistent with known anatomy. Note that the SNR for this data set (approximately 31) is greater than for the other data sets (approximately 20), making it difficult to separate out the effect of the number of DW directions used in the encoding scheme.

Discussion

We have shown that the CSD method presented here can significantly improve the robustness of the spherical deconvolution technique, and therefore of the estimated fibre orientations present in each voxel. This is especially important for fibre-tracking applications that rely on accurate estimates of white matter orientation. With CSD, white matter fibre orientations can be estimated to within 3.5° from a typical *in vivo* acquisition ($b=3000 \text{ s/mm}^2$, SNR=30, for a

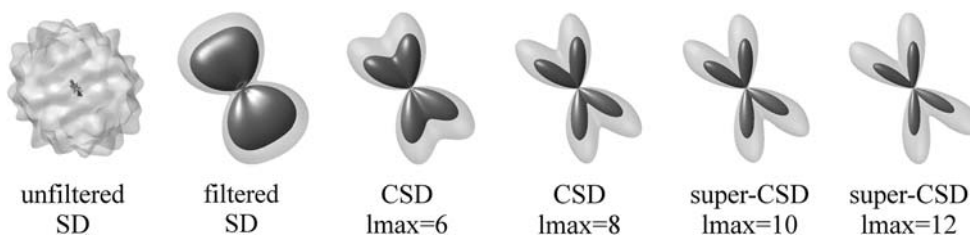


Fig. 4. Effect of l_{\max} on the reconstructed FOD using $b=1000 \text{ s/mm}^2$ data (cf. row 4, Fig. 2). The opaque surface corresponds to the mean FOD over 100 noise realisations, whereas the transparent surface corresponds to the mean +2 standard deviations. Other parameters were SNR=20, separation angle 60° , 60 DW directions, $\lambda=1$, $\tau=10\%$ of mean initial FOD amplitude.

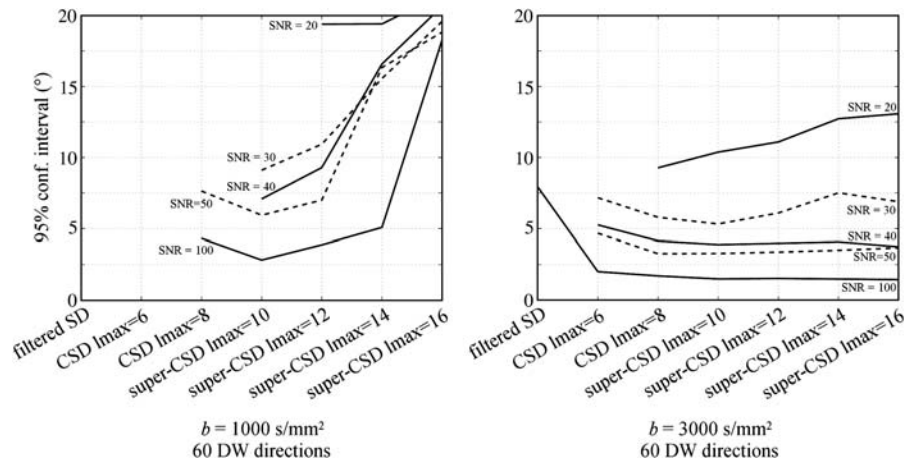


Fig. 5. Simulation results showing the effect of SNR and l_{\max} on the precision of the peak orientations extracted from the reconstructed FOD. Each line corresponds to the 95% confidence interval for the deviation angle between the known and estimated fibre orientation for a particular simulated SNR. Note that the 95% confidence intervals are plotted only if the success rate (see Methods) was at least 95%. Left: results at $b = 1000 \text{ s/mm}^2$. Right: results at $b = 3000 \text{ s/mm}^2$. Other parameters were separation angle = 50° , 60 DW directions, $\lambda = 1$, $\tau = 10\%$ of mean initial FOD amplitude. Every other line is displayed as dashed purely for ease of reading the graph.

90° crossing). The benefits of the method are clear at both b -values investigated, and particularly so for the $b = 1000 \text{ s/mm}^2$ case.

The *a priori* knowledge that the FOD is positive semi-definite provides sufficient extra information that it becomes possible to robustly estimate more parameters than were actually measured (this is known as super-resolution in the field of astrophysics). According to our simulation results and the *in vivo* bootstrap

analysis, it is possible to robustly estimate the 91 parameters required for super-CSD with $l_{\max} = 12$ from a 60 DW direction data set. The advantage of using higher values of l_{\max} is that this makes it possible to resolve smaller separation angles (Fig. 6). Moreover, for sufficiently small separation angles, using super-CSD with $l_{\max} = 10$ (66 parameters) provides more precise peak orientation estimates than using CSD with $l_{\max} = 8$ (45 parameters).

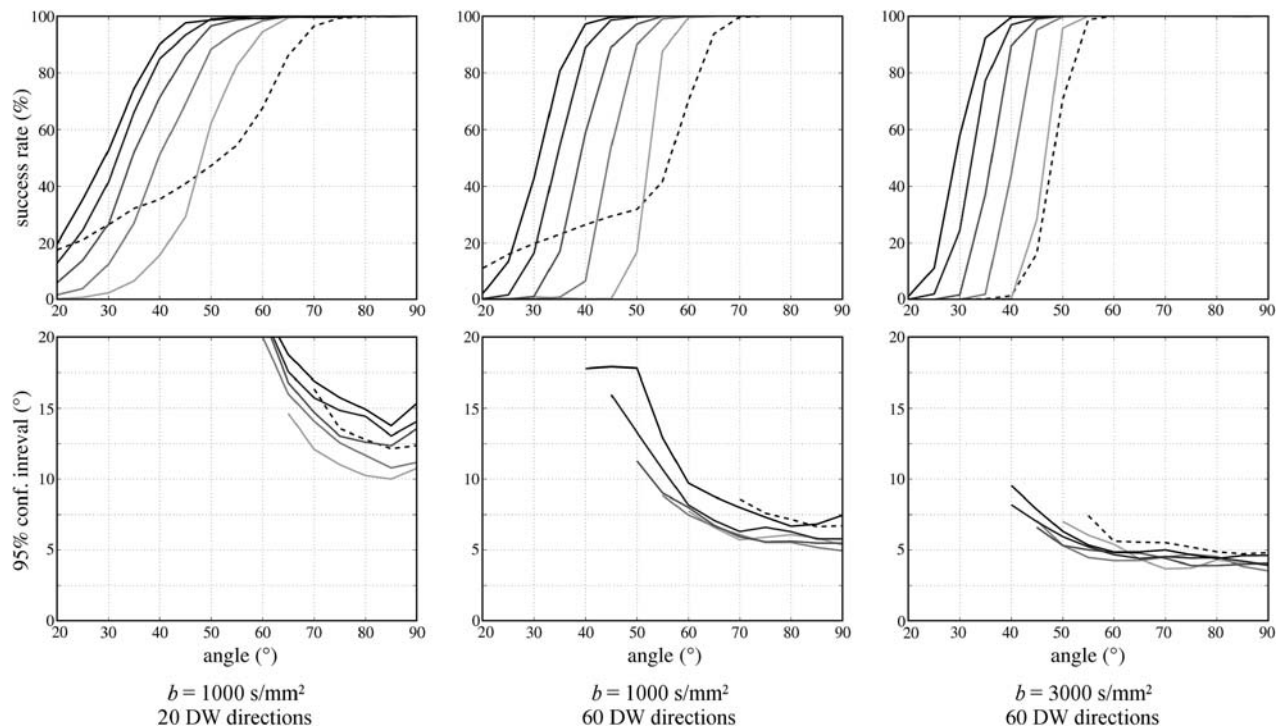


Fig. 6. Simulation results showing the effect of separation angle (x-axis) and l_{\max} on the success rate (see Methods) and precision of the peak orientations extracted from the reconstructed FOD. Top: success rate. Bottom: 95% confidence interval for the deviation angle between the known and estimated fibre orientation. Note that the 95% confidence intervals are plotted only if the success rate was at least 95%. Left: results at $b = 1000 \text{ s/mm}^2$, 20 DW directions. Middle: results at $b = 1000 \text{ s/mm}^2$, 60 DW directions. Right: results at $b = 3000 \text{ s/mm}^2$, 60 DW directions. Dashed line: filtered SD. Solid lines: CSD with l_{\max} ranging from 4 (light grey) to 12 (black) for the 20 DW direction results, and from 6 (light grey) to 16 (black) for the 60 DW direction results. Other parameters were SNR = 30, $\lambda = 1$, $\tau = 10\%$ of mean initial FOD amplitude.

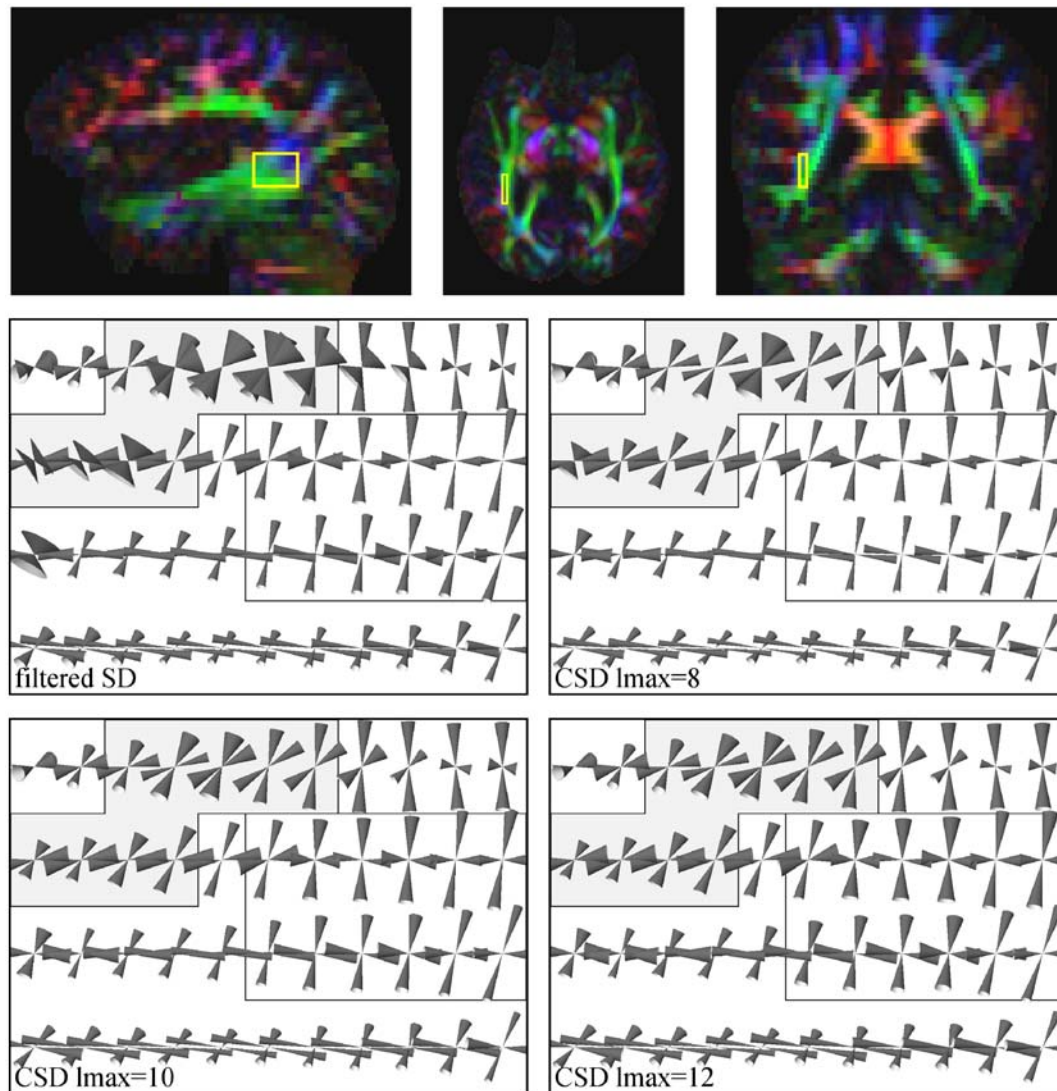


Fig. 7. Cones of uncertainty, representing the 95% confidence interval of the deviation angle, obtained using the bootstrap method from data set B for the region of interest highlighted on the color-coded eigenvector map (top row). The region contains fibres from the inferior longitudinal fasciculus (running anterior-posterior) and the arcuate fasciculus (running inferior-superior). For each subplot, the FODs were estimated using filtered SD with $l_{\max}=8$ (middle left), CSD with $l_{\max}=8$ (middle right), super-CSD with $l_{\max}=10$ (bottom left) and super-CSD with $l_{\max}=12$ (bottom right). Table 1 provides the average 95% confidence interval of the deviation angle for the two groups of voxels highlighted in each subplot. These voxels were chosen on the basis of containing two strong fibre orientations, and grouped according to the angle between these orientations. In the first region, the separation angle between the two main fibre populations is relatively shallow (in light grey). In the second region (in white), the angle is relatively wide.

As implied by the previous point, the precision of the estimated peak orientations was found to be dependent on the angle separating the two fibre populations (Fig. 6). As might be expected, the

Table 1
Deviation angle over 500 bootstrap iterations

	Shallow angle voxels	Wide angle voxels
Filtered SD	25.6°	9.4°
CSD $l_{\max}=8$	14.0°	8.2°
Super-CSD $l_{\max}=10$	13.2°	10.2°
Super-CSD $l_{\max}=12$	13.6°	11.3°

95% confidence intervals for the deviation angle between the mean and estimated peak orientations over 500 bootstrap iterations using data set B, for the two groups of voxels highlighted in Fig. 7.

precision is highest when the two fibre orientations are maximally separated (i.e. perpendicular), and drops as it becomes more difficult to resolve the two orientations. This effect is likely to be common to all algorithms that provide fibre orientations by extracting peak orientations. It is therefore important to take this effect into consideration, in particular if these orientations are to be used in further processing stages such as tractography.

As can be seen from Fig. 1, the reconstructed FOD is relatively insensitive to small changes in the regularisation parameter λ for the constraint on negative values. It was therefore possible to determine a value for λ empirically that would produce reliable results; the actual value used in this study was chosen such that the negative lobes were attenuated to levels insignificant compared to the positive lobes. Moreover, the value chosen from the simulations was found to be suitable for a range of different

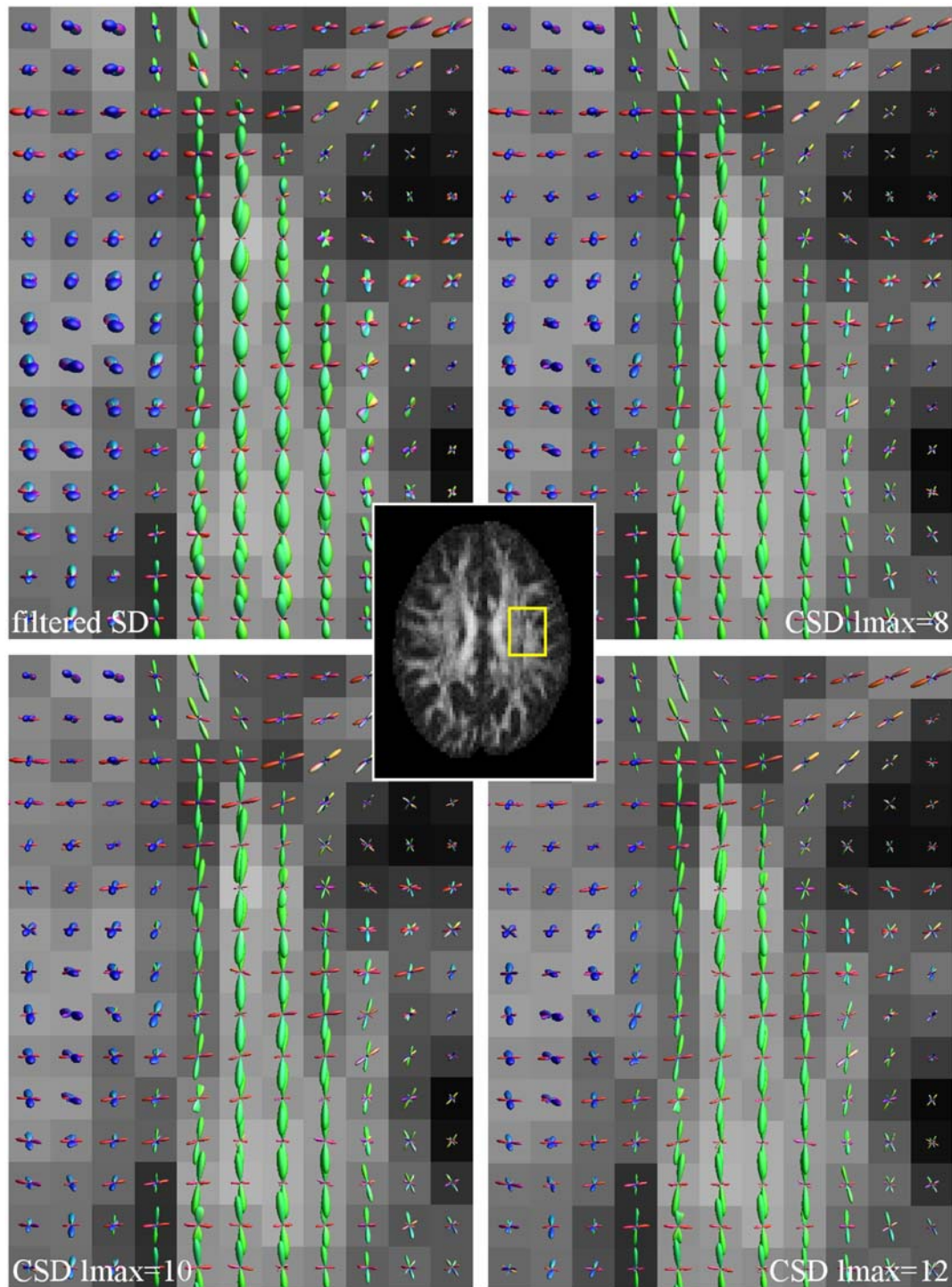


Fig. 8. Results from data set A ($b=3000$ s/mm², 60 DW directions) in the centrum semiovale (location shown on FA map in middle). The estimated FOD is shown in each voxel as a surface rendered plot. In each case, the main contributing fibre tracts can be identified: the corona radiata running in the inferior-superior direction (in blue), the superior longitudinal fasciculus (in green) and the commissural projections from the corpus callosum (in red). Top left: filtered SD with $l_{\max}=8$; top right: CSD with $l_{\max}=8$; bottom left: super-CSD with $l_{\max}=10$; bottom right: super-CSD with $l_{\max}=12$.

experimental conditions, as illustrated by the inclusion of data from three different scanners. More objective methods for finding the optimal value of λ are available (such as the L-curve criterion; Hansen, 1994). Given the robustness of the empirical value used, such an approach was not deemed necessary.

Fig. 1 also shows that using large values of λ has a detrimental effect on the angular resolution of the estimated FOD. Increasing λ is akin to applying the non-negativity constraint more strictly. This suggests that using a ‘soft’ constraint (i.e. penalising negative values in the FOD) may be advantageous over using a ‘hard’

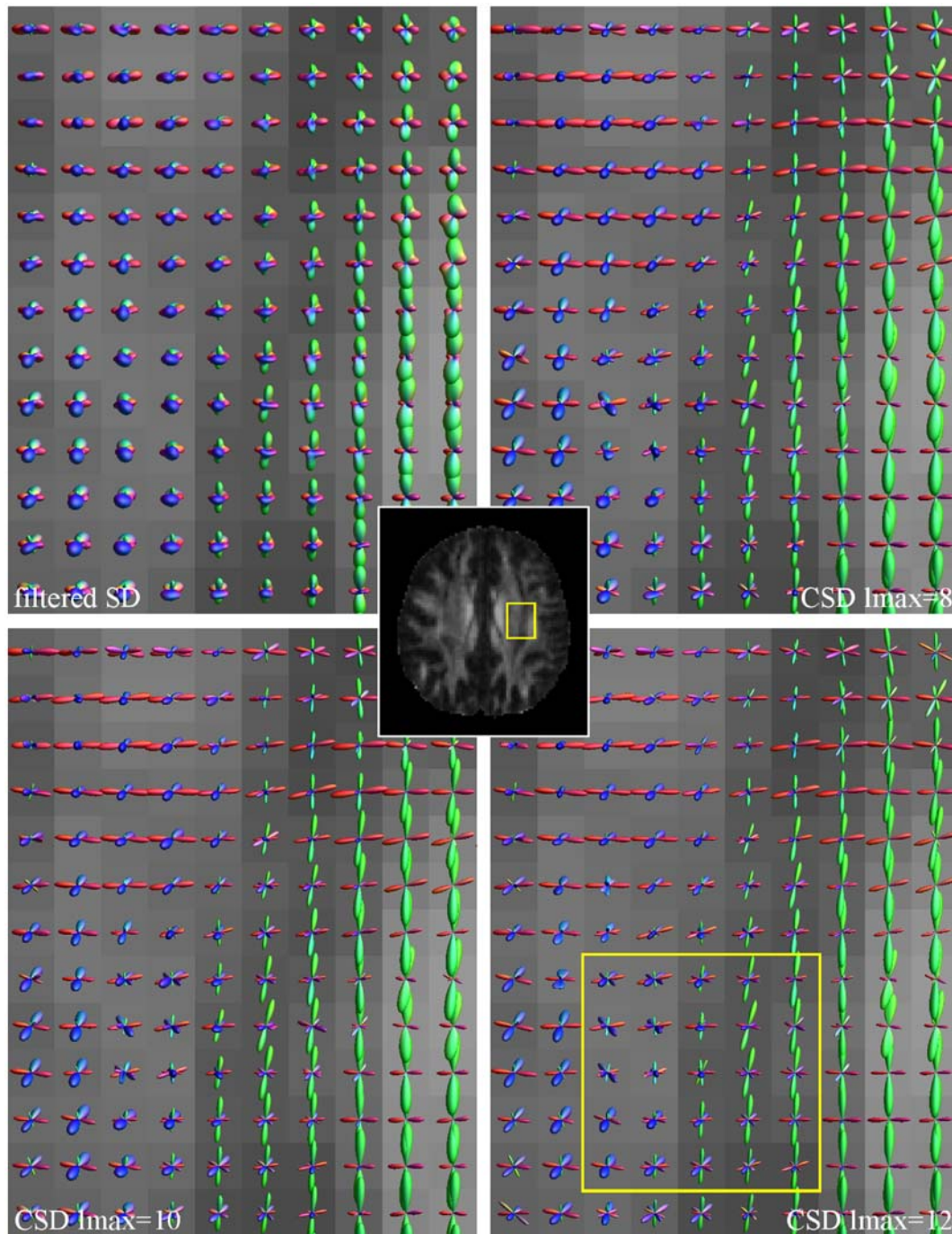


Fig. 9. Results from data set C ($b=1000$ s/mm², 60 DW directions) in the centrum semiovale (location shown on FA map in middle). The estimated FOD is shown in each voxel as a surface rendered plot. In each case, the main contributing fibre tracts can be identified: the corona radiata running in the inferior-superior direction (in blue), the superior longitudinal fasciculus (in green) and the commissural projections from the corpus callosum (in red). Top left: filtered SD with $l_{\max}=8$; top right: CSD with $l_{\max}=8$; bottom left: super-CSD with $l_{\max}=10$; bottom right: super-CSD with $l_{\max}=12$. Some spurious fibre orientations can be observed in the region highlighted (cf. Fig. 8).

constraint (i.e. where negative values in the FOD are explicitly forbidden). Moreover, as the FOD is expressed using spherical harmonics, it would be expected to contain some negative lobes due to the spherical equivalent of Gibbs's ringing. In the Cartesian case, a delta function expressed as a truncated Fourier series becomes a sinc function (the point spread function), which contains

negative side lobes. The same effect can be seen in the spherical case: the representation of a delta function (i.e. the FOD for a single fibre population) expressed as a truncated SH series also contains small negative side lobes. Forcing the algorithm to completely eliminate these lobes by using a 'hard' constraint may therefore be counter-productive.

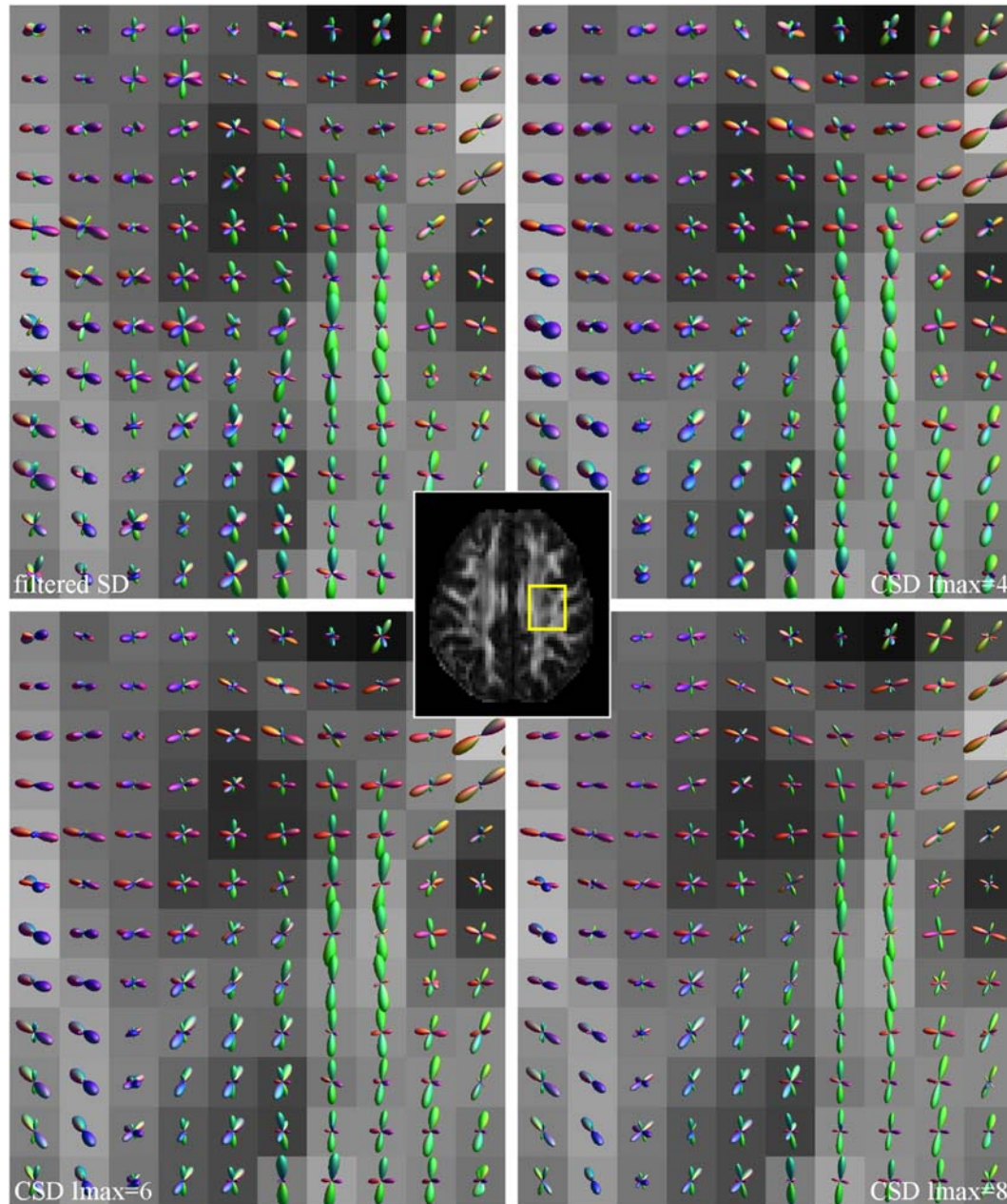


Fig. 10. Results from data set D ($b=1000$ s/mm², 20 DW directions) in the centrum semiovale (location shown on FA map in middle). The estimated FOD is shown in each voxel as a surface rendered plot. Top left: filtered SD with $l_{\max}=4$; top right: CSD with $l_{\max}=4$; bottom left: super-CSD with $l_{\max}=6$; bottom right: super-CSD with $l_{\max}=8$.

The threshold τ was introduced to improve the stability of the super-CSD algorithm. As shown in Fig. 1, the value that was chosen in this study does not introduce any significant differences in the reconstructed FOD. It should be noted that the need for this parameter is specific to this particular implementation. It may be possible to perform super-CSD using other methods that do not require such a parameter (for example, using a Bayesian framework).

Recent studies have shown that correcting for the Rician noise bias that is inherent in low SNR MR measurements improved the quality of spherical deconvolution results (Alonso Clarke et al., 2006). Such a pre-processing step could easily be combined with the present regularisation technique, and may further improve the

robustness of the results. This is, however, beyond the scope of this study.

The data presented here (see Figs. 8, 9 and 10) emphasise the need for high b -values to better resolve crossing fibres with spherical deconvolution. The effect of increasing the b -value is to accentuate the difference in DW signal attenuation along the fibre axis relative to that along perpendicular orientations; in other words, it produces a ‘flatter’ response function. This introduces more orientation contrast when multiple orientations are present, and improves the stability of the algorithm. This is confirmed in this study both by the simulation results and by the *in vivo* data: the FODs reconstructed using the $b \sim 3000$ s/mm² data are

less sensitive to noise, and have sharper features than their $b \sim 1000$ s/mm² counterparts.

Although the orientation contrast increases with b -value, there will be a corresponding reduction in the DW signal intensity. The optimal b -value should therefore provide the best orientation contrast to noise ratio. It is not possible however, to estimate this optimal b -value from the results presented here, as the data acquired did not cover a sufficient range of b -values, and realistic estimates of the response function can only be obtained from such data.

The value of l_{\max} determines the maximum achievable angular resolution: a larger l_{\max} produces a narrower ‘angular point spread function’ (Hess et al., 2006). Super-CSD makes it possible to use very large values of l_{\max} (provided a sufficient number of directions N are used for the constraint matrix \mathbf{P} —see Eq. (4)). However, this will also be accompanied by an increase in noise sensitivity. In practice, the optimal l_{\max} will be determined by the trade-off between noise sensitivity and angular resolution. For example, according to Fig. 5, for SNR=30, the optimal value of l_{\max} would be 10 at $b=1000$ s/mm², and 12 at $b=3000$ s/mm².

The results of our previous work with the filtered SD method seemed to indicate that lower b -value data would not be suitable for spherical deconvolution (Tournier et al., 2004). However, the improved results obtained using CSD show that those data can in fact be used, although with lower quality results than at $b=3000$ s/mm². This is demonstrated both by the simulations (Figs. 4, 5 and 6) and by the *in vivo* results obtained from data set C, acquired with a b -value of 1000 s/mm²: the FODs obtained with CSD are much more sharply defined than those obtained with filtered SD (Fig. 9). Moreover, the super-CSD method makes it possible to process DW data that were acquired using a relatively small number of directions. The simulation results show that super-CSD can be applied to $b=1000$ s/mm², 20 DW direction data, although with lower quality results (Fig. 6). Super-CSD was also applied to data set D, which was initially intended for diffusion tensor analysis, and thus acquired at $b=1000$ s/mm² using a 20 DW direction scheme (Fig. 10). With such a low number of measurements, the maximum harmonic order that can be achieved with filtered SD is $l_{\max}=4$ (15 parameters), which produces poorly resolved, relatively noisy FODs. However, with super-CSD, it becomes possible to estimate the 45 parameters required for $l_{\max}=8$. The CSD and super-CSD methods therefore make it possible to apply the spherical deconvolution technique retrospectively to data that might have been intended for use in diffusion tensor analyses, and which were thus acquired with lower b -values and/or number of DW directions than would be recommended for spherical deconvolution.

The improved angular resolution and fibre orientation estimates made possible by the proposed CSD and super-CSD techniques are of great potential benefit for probabilistic fibre tracking applications, which rely on accurate estimates of the FOD. The ability to resolve fibre orientations that are separated by smaller angles should improve the accuracy of tracking results for tracts that pass through or close to other tracts that are similarly oriented. In addition, the sharper peaks in the FOD will lead to improved spatial localisation of the connectivity maps generated using probabilistic fibre-tracking techniques (e.g. Behrens et al., 2003; Parker and Alexander, 2005; Behrens et al., 2003), as the algorithm will have a smaller range of orientations to sample at each step.

Conclusion

We have presented a novel method to perform spherical deconvolution that includes a constraint on the presence of negative values in the fibre orientation distribution (FOD), which are physically impossible. The addition of this *a priori* information also permits the use of super-resolution, whereby the FOD is estimated with higher angular resolution than would otherwise be possible from the data alone. This improves the reliability of the resulting estimates of the FOD within each voxel, and makes it possible to resolve fibre orientations separated by smaller angles than was previously possible with spherical deconvolution, by increasing the achievable angular resolution. As shown in the results, this makes it possible to use $b \sim 1000$ s/mm² data, which were previously believed to be unsuitable. The improvement in the estimation of the fibre orientations made possible by this method may lead to the development of more robust tractography algorithms, capable of tracking reliably through regions containing multiple fibre populations.

Acknowledgments

We thank David Gadian and the Radiology and Physics Unit at the UCL Institute of Child Health, University College London, London, UK, for helpful discussion and for the use of *in vivo* data. We also thank Olga Ciccarelli and co-workers at the UCL Institute of Neurology, University College London, London, UK, for providing *in vivo* data set C. We are grateful to the National Health and Medical Research Council (NHMRC) and Austin Health for support.

Appendix A

A.1. Spherical harmonic transform

The matrices \mathbf{Q} and \mathbf{P} (Eqs. (3) and (4)) perform the mapping from SH coefficients to amplitudes along a given set of orientations. This operation can be simplified using the intrinsic symmetry properties of the diffusion process. As diffusion is symmetric about the origin, we only need to consider the even orders. In addition, as the functions involved are real, their SH representations exhibit conjugate symmetry, halving the number of parameters to be estimated. The elements of \mathbf{Q} and \mathbf{P} used in this study were chosen to satisfy these properties, and were therefore defined as follows:

$$(\mathbf{P}, \mathbf{Q})_{ij} = \begin{cases} \text{Re}(Y_l^m(\theta_i, \phi_i)) & m \geq 0 \\ \text{Im}(Y_l^m(\theta_i, \phi_i)) & m < 0 \end{cases} \quad (8)$$

$$m \in [-l, l], \quad l \text{ even}$$

$$j = 1/2 l(l+1) + m$$

where $Y_l^m(\theta, \phi)$ are the standard spherical harmonic functions, and $\{\theta_i, \phi_i\}$ is the set of orientations of interest.

A.2. Rotational harmonic coefficients

In addition to the symmetry properties mentioned above, the axial symmetry of the response function $R(\theta)$ implies that only the $m=n=0$ rotational harmonic coefficients are non-zero, so that \mathbf{R}_j is

a simple multiple of the identity matrix. Eq. (1) can therefore be re-written as:

$$s_l = r_l f_l \quad (9)$$

where r_l is now a real scalar constant, whose value can be computed easily using the following procedure.

If the FOD $F(\theta, \phi)$ was a unit delta function aligned with the z -axis, then the DW signal $S(\theta, \phi)$ measured should be identical to the response function $R(\theta)$. In other words, if f_l corresponds to a delta function, then s_l must correspond to the response function. In this case, as both functions are axially symmetric, all $m \neq 0$ coefficients are zero. Therefore, r_l can be computed by simple scalar division of the l th order, $m=0$ SH coefficients of $R(\theta)$ by the corresponding coefficient for a delta function.

The matrix \mathbf{R} in Eq. (3) is therefore diagonal, with $\mathbf{R}_{jj} = r_l$, where $j = \frac{1}{2}l(l+1) + m$ (cf. Eq. (8)).

References

- Alexander, D.C., Barker, G.J., Arridge, S.R., 2002. Detection and modelling of non-Gaussian apparent diffusion coefficient profiles in human brain data. *Magn. Reson. Med.* 48, 331–340.
- Alonso Clarke, R., Scifo, P., Dell'Acqua, F., Rizzo, G., Scotti, G., Fazio, F., 2006. Noise correction on rician distributed data for fiber orientation estimators. *Proceedings of the 14th Annual Meeting of the ISMRM*, Seattle, USA, p. 345.
- Anderson, A.W., 2005. Measurement of fiber orientation distributions using high angular resolution diffusion imaging. *Magn. Reson. Med.* 54, 1194–1206.
- Assaf, Y., Freidlin, R.Z., Rohde, G.K., Basser, P.J., 2004. New modeling and experimental framework to characterize hindered and restricted water diffusion in brain white matter. *Magn. Reson. Med.* 52, 965–978.
- Basser, P.J., 1995. Inferring microstructural features and the physiological state of tissues from diffusion-weighted images. *NMR Biomed.* 8, 333–344.
- Basser, P.J., Mattiello, J., Le Bihan, D., 1994. MR diffusion tensor spectroscopy and imaging. *Biophys. J.* 66, 259–267.
- Behrens, T.E.J., Woolrich, M.W., Jenkinson, M., Johansen-Berg, H., Nunes, R.G., Clare, S., Matthews, P.M., Brady, J.M., Smith, S.M., 2003. Characterization and propagation of uncertainty in diffusion-weighted MR imaging. *Magn. Reson. Med.* 50, 1077–1088.
- Behrens, T.E.J., Johansen Berg, H., Jbabdi, S., Rushworth, M.F.S., Woolrich, M.W., 2007. Probabilistic diffusion tractography with multiple fibre orientations: what can we gain? *NeuroImage* 34, 144–155.
- Callaghan, P.T., Eccles, C.D., Xia, Y., 1988. NMR microscopy displacements: k-space and q-space imaging. *J. Phys. E* 21, 820.
- Clark, C.A., Le Bihan, D., 2001. Water diffusion compartmentation and anisotropy at high b values in the human brain. *Magn. Reson. Med.* 44, 852–859.
- Cohen, Y., Assaf, Y., 2002. High b-value q-space analyzed diffusion-weighted MRS and MRI in neuronal tissues—A technical review. *NMR Biomed.* 15, 516–542.
- Conturo, T.E., Lori, N.F., Cull, T.S., Akbudak, E., Snyder, A.Z., Shimony, J.S., McKinstry, R.C., Burton, H., Raichle, M.E., 1999. Tracking neuronal fiber pathways in the living human brain. *Proc. Nat. Acad. Sci.* 96, 10422–10427.
- Frank, L.R., 2002. Characterisation of anisotropy in high angular resolution diffusion-weighted MRI. *Magn. Reson. Med.* 47, 1083–1099.
- Hansen, P.C., 1994. Regularization tools: a MATLAB package for analysis and solution of discrete ill-posed problems. *Numer. Algorithms* 6, 1–35.
- Healy, D.M., Hendriks, H., Kim, P.T., 1998. Spherical deconvolution. *J. Multivar. Anal.* 67, 1–22.
- Hess, C.P., Mukherjee, P., Han, E.T., Xu, D., Vigneron, D.B., 2006. Q-ball reconstruction of multimodal fiber orientations using the spherical harmonic basis. *Magn. Reson. Med.* 56, 104–117.
- Hong, X., Anderson, A.W., Ding, Z., 2006. Resolve fiber orientation ambiguity using HARD imaging. *Proceedings of the 14th Annual Meeting of the ISMRM*, Seattle, USA, p. 2728.
- Hosey, T., Williams, G., Anson, R., 2005. Inference of multiple fiber orientations in high angular resolution diffusion imaging. *Magn. Reson. Med.* 54, 1480–1489.
- Jansons, K.M., Alexander, D.C., 2003. Persistent angular structure: new insights from diffusion MRI data. *Inverse Probl.* 19, 1031–1046.
- Jones, D.K., 2003. Determining and visualizing uncertainty in estimates of fiber orientation from diffusion tensor MRI. *Magn. Reson. Med.* 49, 7–12.
- Jones, D.K., Horsfield, M.A., Simmons, A., 1999. Optimal strategies for measuring diffusion in anisotropic systems by magnetic resonance imaging. *Magn. Reson. Med.* 42, 515–525.
- Lin, C.P., Wedeen, V.J., Chen, J.H., Yao, C., Tseng, W.Y.I., 2003. Validation of diffusion spectrum magnetic resonance imaging with manganese-enhanced rat optic tracts and ex vivo phantoms. *NeuroImage* 19, 482–495.
- Mori, S., Crain, B.J., Chacko, V.P., van Zijl, P.C.M., 1999. Three-dimensional tracking of axonal projections in the brain by magnetic resonance imaging. *Ann. Neurol.* 45, 265–269.
- Mulkern, R.V., Gudbjartsson, H., Westin, C.F., Zengingonul, H.P., Gartner, W., Guttman, C.R., Robertson, R.L., Kyriakos, W., Schwartz, R., Holtzman, D., Jolesz, F.A., Maier, S.E., 1999. Multi-component apparent diffusion coefficients in human brain. *NMR Biomed.* 12, 51–62.
- Özarslan, E., Shepherd, T.M., Vemuri, B.C., Blackband, S.J., Mareci, T.H., 2006. Resolution of complex tissue microarchitecture using the diffusion orientation transform (DOT). *NeuroImage* 31, 1086–1103.
- Parker, G.J., Alexander, D.C., 2005. Probabilistic anatomical connectivity derived from the microscopic persistent angular structure of cerebral tissue. *Philos. Trans. R. Soc. B* 360, 893–902.
- Parker, G.J.M., Wheeler-Kingshott, C.A.M., Barker, G.J., 2002. Estimating distributed anatomical connectivity using fast marching methods and diffusion tensor imaging. *IEEE Trans. Med. Imag.* 21, 505–512.
- Pierpaoli, C., Barnett, A., Pajevic, S., Chen, R., Penix, L., Virta, A., Basser, P.J., 2001. Water diffusion changes in Wallerian degeneration and their dependence on white matter architecture. *NeuroImage* 13, 1174–1185.
- Reese, T.G., Heid, O., Weisskoff, R.M., Wedeen, V.J., 2003. Reduction of eddy-current-induced distortion in diffusion MRI using a twice-refocused spin echo. *Magn. Reson. Med.* 49, 177–182.
- Starck, J.L., Pantin, E., Murtagh, F., 2002. Deconvolution in astronomy: A review. *Publ. Astron. Soc. Pac.* 114, 1051–1069.
- Symms, M.R., Barker, G.J., Franconi, F., Clark, C.A., 1997. Correction of eddy-current induced distortions in diffusion-weighted echo-planar images with a two-dimensional registration technique. *Proceedings of the 5th Annual Meeting of the ISMRM*, Vancouver, Canada, p. 1723.
- Tournier, J.D., Calamante, F., Gadian, D.G., Connelly, A., 2003. Diffusion-weighted MRI fibre-tracking using a front evolution algorithm. *NeuroImage* 20, 276–288.
- Tournier, J.D., Calamante, F., Gadian, D.G., Connelly, A., 2004. Direct estimation of the fibre orientation density function from diffusion-weighted MRI data using spherical deconvolution. *NeuroImage* 23, 1176–1185.
- Tournier, J.D., Calamante, F., Connelly, A., 2005. Improved characterisation of crossing fibres: optimisation of spherical deconvolution parameters using a minimum entropy principle. *Proceedings of the 13th Annual Meeting of the ISMRM*, Miami, USA, p. 384.
- Tuch, D.S., 2004. Q-ball imaging. *Magn. Reson. Med.* 52, 1358–1372.
- Tuch, D.S., Reese, T.G., Wiegell, M.R., Makris, N., Belliveau, J.W., Wedeen, V.J., 2002. High angular resolution diffusion imaging reveals intravoxel white matter fiber heterogeneity. *Magn. Reson. Med.* 48, 577–582.
- Wedeen, V.J., Hagmann, P., Tseng, W.Y., Reese, T.G., Weisskoff, R.M., 2005. Mapping complex tissue architecture with diffusion spectrum magnetic resonance imaging. *Magn. Reson. Med.* 54, 1377–1386.
- Zhan, W., Yang, Y., 2006. How accurately can the diffusion profiles indicate multiple fiber orientations? A study on general fiber crossings in diffusion MRI. *J. Magn. Reson.* 183, 193–202.